Chemical Science

ROYAL SOCIETY OF CHEMISTRY

EDGE ARTICLE

View Article Online
View Journal

Cite this: DOI: 10.1039/d6sc01783e

All publication charges for this article have been paid for by the Royal Society of Chemistry

Regulation of local chemistry in O3-type layered oxide cathodes for practical sodium-ion batteries

Tongtong Huo,[a] Qian Yang,[a] Genliang Yu,[a] Mingyue Li,[a] Xuejie Bai,[a] Ting Lv,[a] Xiaobo Zhang,[a] Jie Xu,[a] Kai Liu,[a] Xunzhu Zhou,[b] Xin Tan,[bc] Lin Li,*[bc] Kaixiang Lei*[a] and Shijian Zheng*[a]

O3-type layered oxide cathodes have emerged as promising candidates for advanced sodium-ion batteries (SIBs) due to their high theoretical specific capacity. However, undesirable phase transitions, irreversible O_2 release, and transition metal (TM) ion dissolution severely deteriorate their long-cycle stability. Herein, a cation–anion dual-site high-entropy doping strategy is proposed to modulate the local chemistry of O3-type layered oxide cathodes, aiming to enhance the covalency of TM–O bonds. The robust covalent TM–O bonds can effectively suppress adverse phase transitions, inhibit irreversible oxygen redox reactions, and reduce TM^{n+} dissolution. Consequently, $NaNi_{0.25}Fe_{0.14}Mn_{0.3}Li_{0.1}Ti_{0.15}Cu_{0.03}Zn_{0.03}O_{1.94}F_{0.06}$ (HEO) delivers a high specific capacity of 152.27 mA h g^{-1} and a capacity retention of 73.69% after 500 cycles. More importantly, HEO exhibits impressive temperature tolerance, superior air stability and acceptable full-cell performance, demonstrating its huge potential for practical SIBs application. This work develops a versatile cation–anion dual-site high-entropy doping strategy to modulate the local chemistry of O3-type layered oxide cathodes, furnishing a robust foundation for advancing cathode materials for practical SIBs.

Received 3rd March 2026
Accepted 10th April 2026

DOI: 10.1039/d6sc01783e

rsc.li/chemical-science

Introduction

Sodium-ion batteries (SIBs) hold great promise as a pivotal technology for large-scale energy storage systems due to their abundant resource reserves and low production costs.[1–3] As a core component of SIBs, cathode materials have a critical impact on their electrochemical performance, technological development potential, and practical application prospects.[4] Among the discovered cathode materials, O3-type layered oxide cathodes (Na_xTMO_2, where $x > 0.7$, TM represents transition metal) demonstrate broad application prospects due to their high theoretical specific capacity.[5,6] However, during the charge/discharge process of the O3-NFM (O3-$NaNi_{0.4}Fe_{0.2}Mn_{0.4}O_2$) cathode, the deintercalation of Na^+ and the oxidation of TM^{n+} induce continuous variations in the unit cell parameters. In particular, under high-voltage conditions exceeding 4.0 V, this triggers an unfavorable P3 → O3′ phase transition, thereby resulting in severe volume changes.[7,8] Furthermore, the excessive oxidative participation of lattice oxygen exposes the inherently weak TM–O bonds to a higher risk of disruption: it not only readily forms O–O dimers, ultimately resulting in the irreversible release of lattice oxygen in the form of O_2, but the cleavage of TM–O bonds also creates conditions for the additional irreversible dissolution of TM^{n+}.[9–11] This leads to a reduction in the number of active TM sites, exacerbates interfacial side reactions, and triggers the initiation of intragranular cracks.[12,13] Collectively, these complex detrimental effects ultimately induce an irreversible phase transition of the cathode material from a layered structure to a rock-salt phase, resulting in permanent structural damage with fast capacity degradation.[14,15]

In general, the TM–O bonds serve as the core structural framework of layered oxide cathode materials, and the insufficiency of their covalency is the intrinsic cause triggering the aforementioned performance degradation issues.[16–18] Therefore, regulating the covalency of TM–O bonds is regarded as an effective strategy to boost the sodium storage performance of O3-type layered oxide cathodes.[19–22] To date, element doping, as a facile and efficient modification strategy, has been extensively adopted to optimize the local chemistry of O3-type layered oxide cathode materials.[23–25] Nevertheless, conventional single/double-element doping strategies exhibit certain limitations, failing to simultaneously address multiple issues including phase structure distortion, lattice oxygen release, and transition

[a]Tianjin Key Laboratory of Materials Laminating Fabrication and Interface Control Technology, School of Materials Science and Engineering, Hebei University of Technology, Tianjin 300401, China. E-mail: kaixianglei@hebut.edu.cn; sjzheng@hebut.edu.cn

[b]Institute for Carbon Neutralization Technology, College of Chemistry and Materials Engineering, Wenzhou University, Wenzhou, Zhejiang 325035, China. E-mail: linli@wzu.edu.cn

[c]Zhejiang Provincial Key Laboratory of Advanced Battery Materials and Technology, Wenzhou University Technology Innovation Institute for Carbon Neutralization, Zhejiang 325035, China

metal ion dissolution.[7,26] In recent years, the high-entropy doping strategy, relying on the synergistic effect of multiple elements, has demonstrated unique advantages in precisely regulating the local chemistry of layered oxide cathode materials and stabilizing the lattice framework, thereby providing a novel paradigm for the performance breakthrough in electrode materials.[27,28] However, most existing studies on high-entropy doping are confined to the modification of cation sites, failing to give full play to the synergistic regulation effect of both anions and cations.[29–32] Its modulation effect on the covalency of TM–O bonds is limited, making it difficult to fundamentally overcome the performance degradation bottleneck of O3-type layered oxide cathodes.[33,34]

Herein, we propose a cation–anion dual-site high-entropy doping strategy, which is designed to regulate the local chemical environment of O3-type layered oxide cathodes and enhance the covalency of TM–O bonds *via* the synergistic doping effects of multi-elements at cation sites (Li, Ti, Cu, and Zn) and anion sites (F). The enhanced covalency of TM–O bonds can effectively simplify the phase transition process of O3-type layered oxide cathodes during the charge/discharge process and suppress the occurrence of irreversible phase transitions, thereby significantly improving the structural integrity of electrode materials. Furthermore, it can effectively inhibit the irreversible oxygen redox reactions and the dissolution of transition metal ions under high-voltage operating conditions. Benefiting from the aforementioned advantages, the designed O3-type $NaNi_{0.25}Fe_{0.14}Mn_{0.3}Li_{0.1}Ti_{0.15}Cu_{0.03}Zn_{0.03}O_{1.94}F_{0.06}$ (HEO) material exhibits excellent cycling stability, favorable temperature tolerance, outstanding air stability, as well as superior full-cell performance, which fully verifies its potential for practical applications. The cation–anion dual-site high-entropy doping strategy proposed in this study provides a novel and universal paradigm for regulating the local chemical environment of O3-type layered oxide cathodes.

Results and discussion

Conventional O3-type layered oxide cathodes suffer from adverse phase transitions, irreversible oxygen release, and transition metal ion dissolution during cycling (Fig. 1a). These issues further induce the formation of microcracks inside the material, impair its structural integrity, and ultimately lead to the degradation of electrochemical performance.[15] In general, the covalency of TM–O bonds is closely correlated with the structural stability of the O3-type layered oxide cathodes. Herein, a cation–anion dual-site high-entropy doping strategy is proposed to modulate the local chemical environment of O3-type layered oxide cathodes, thereby enhancing the covalency of TM–O bonds and ultimately achieving a breakthrough improvement in sodium storage performance. As shown in Fig. 1b, Li^+ with the $1s^2$ electron configuration and Zn^{2+} with the $3d^{10}$ electron configuration are selected to enhance the local covalent bonding between Ni/Fe/Mn and O.[16,35] This enhancement is achieved through their weak hybridization with O 2p orbitals and the formation of Li/Zn–O–TM bridge-type structures.[36] Ti^{4+} and Cu^{2+} are selected due to their strong-bond-forming characteristics when bonding with O, which create non-positioned "rivets" within the structure and significantly enhance the local covalency of the bonding network.[19,37,38] Additionally, F^- with a smaller ionic radius and higher electronegativity is doped into lattice oxygen sites. The formation of strong and short TM–F bonds leads to an overall contraction of the TM layer, thereby enhancing the orbital overlap between TM

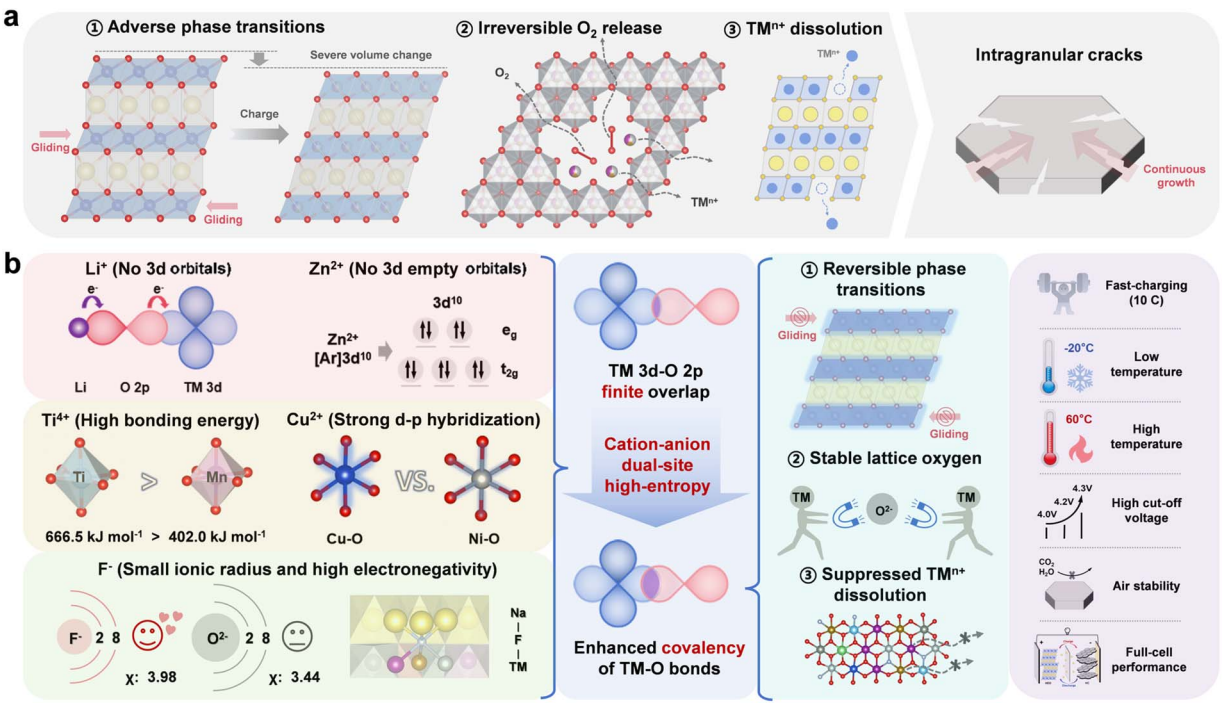

Fig. 1 (a) Challenges of O3-type layered oxide cathodes. (b) Schematic diagrams of the cation–anion dual-site high-entropy doping strategy.

3d and O 2p (Fig. S1, SI).[39–41] The strong TM–F bonds not only enhance structural stability but also, to some extent, influence the Na layer through the TM–F–Na bonding network (Fig. S2 and Table S1, SI).[42] This synergistic enhancement of TM–O covalency is expected to inhibit adverse phase transition processes, suppress irreversible O_2 release, restrain transition metal ion dissolution, and enhance structural stability under multiple application conditions.

To validate our design concept, $NaNi_{0.4}Fe_{0.2}Mn_{0.4}O_2$ (NFM) and $NaNi_{0.25}Fe_{0.14}Mn_{0.3}Li_{0.1}Ti_{0.15}Cu_{0.03}Zn_{0.03}O_{1.94}F_{0.06}$ (HEO) are synthesized *via* a simple solid-phase reaction. As shown in Fig. 2a, the sharp and distinct diffraction peaks indicate that both NFM and HEO can be classified as the O3-type structure (space group *R*-3*m*, PDF #88-0720). Additionally, the presence of NiO diffraction peaks (space group *Fm*-3*m*, PDF #47-1049) is observed in the XRD patterns of NFM, which is attributed to the solubility limit of nickel in the O3 phase.[30] In contrast, HEO is a single-phase solid solution of the O3-type. The detailed structural information for NFM and HEO is revealed *via* X-ray diffraction (XRD) Rietveld refinement (Fig. 2b and c and Tables S2–S4, SI). Compared to NFM, HEO exhibits an expanded *d*(O–Na–O) spacing (increased from 3.158 Å to 3.170 Å) and enlarged octahedral/tetrahedral volumes, which facilitates rapid Na^+ diffusion (Fig. 2d). Furthermore, the synergistic doping of multiple heterogeneous ions has led to a noticeable alteration in the *d*(O–TM–O) spacing. Subsequently, the elemental compositions were measured by inductively coupled plasma optical emission spectroscopy (ICP-OES) and fluoride-ion selective electrode (ISE) methods, and the results were in close accordance with the theoretically designed ratios (Table S5). As illustrated in Fig. 2e, co-doping with multiple heterogeneous ions induces a substantial increase in configurational entropy (from 1.055 R to 1.843 R), a signature that verifies the high-entropy nature of HEO.[41,43]

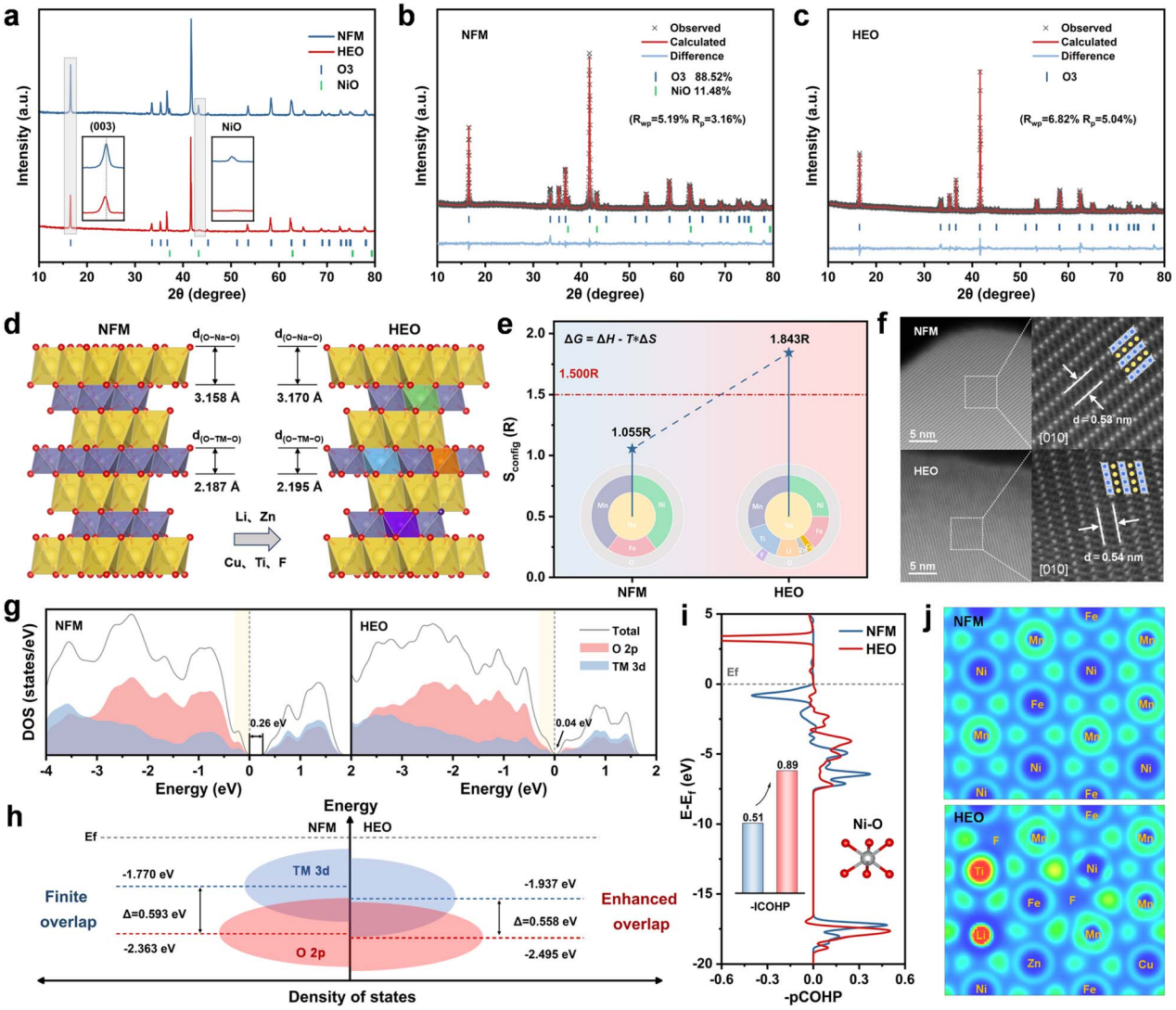

Fig. 2 (a) XRD patterns of NFM and HEO. Rietveld refinement results of (b) NFM and (c) HEO. Schematic diagrams of (d) crystal structure and (e) configurational entropy of NFM and HEO. (f) AC-HAADF-STEM images of NFM and HEO. (g) The density of states and (h) schematic diagrams of the band structure of NFM and HEO. (i) COHP results of Ni–O bonds in NFM and HEO. (j) ELF of the valence electron in TM-layer viewed along the [001] direction.

The morphological and microstructural characterization of NFM and HEO was performed using scanning electron microscopy (SEM) and transmission electron microscopy (TEM). As shown in Fig. S3 (SI), NFM and HEO exhibit similar primary particles with clean surfaces and average particle sizes of about 1 μm. High-resolution transmission electron microscopy (HRTEM) images reveal that both HEO and NFM exhibit the characteristic (003) lattice fringes of the O3 phase, with HEO displaying a larger interplanar spacing (Fig. S4, SI).[14] By spherical aberration corrected scanning transmission electron microscopy (AC-STEM) combined with high-angle annular dark-field (HAADF) imaging (Fig. 2f and S5, SI), an increased interplanar spacing (5.4 Å *vs.* 5.3 Å) is further confirmed in HEO, which is consistent with the increase of the lattice parameter *c*. Furthermore, energy dispersive spectroscopy (EDS) elemental mapping confirms the uniform distribution of each element throughout the bulk phase in NFM and HEO (Fig. S6 and S7, SI).

In general, the stability of the bonds between TM and O is closely related to the sodium storage performance of O3-type layered oxide cathode materials. X-ray absorption near-edge structure (XANES) spectra and Fourier-transformed extended X-ray absorption fine structure (FT-EXAFS) techniques are first employed to reveal the electronic structure and coordination information of transition metal ions in NFM and HEO (Fig. S8 and S9, SI).[44] The initial oxidation states of Ni, Fe, and Mn in both materials are +2, +3, and +4, respectively. Noticeably, the Ni–O, Fe–O, and Mn–O bonds in HEO all exhibit significant shortening, indicating that higher bonding energies enhance structural stability. This sufficiently robust covalent bonding network will significantly improve the sodium storage performance.[20] Subsequently, density functional theory (DFT) calculations are employed to elucidate the impact of the cation–anion dual-site high-entropy doping strategy on the electronic structure. The total density of states (TDOS) in Fig. 2g reveals a markedly narrower band gap near the Fermi level after modification (as marked by the black arrow), indicating enhanced electronic conductivity.[45] As shown in Fig. 2h, the O 2p band center shifted downward in HEO, which implies an increase in the stabilization of the oxygen redox reaction.[32,46] Concurrently, the energy difference between the TM 3d and O 2p band centers was decreased (0.593 eV *vs.* 0.558 eV), corresponding to strengthened hybridization of the TM 3d–O 2p orbitals. Collectively, these results confirm that the cation–anion dual-site high-entropy doping strategy enhances the covalency of TM–O bonds, thereby fortifying the structural stability of the cathode material.[10,47] Furthermore, the Li 2s and Zn 3d orbitals exhibit negligible hybridization with O 2p orbitals near the Fermi level, which is consistent with the design expectations based on our element selection strategy (Fig. S10, SI). The changes in TM–O bonding energies were further quantified by crystal orbital Hamilton population (COHP) analyses (Fig. 2i and S11, SI). Compared to NFM, Ni/Fe/Mn–O bonds in HEO exhibit higher – ICOHP values, with more bonding-filled orbitals and anti-bonding empty orbitals. This observation indicates that the proposed doping strategy can effectively enhance the covalency of TM–O bonds.[21,48–50] Subsequently, the electronic localization function (ELF) was employed to characterize the degree of charge localization around the constituent ions within the crystal structure (Fig. 2j). The localized charges on the O and TM atoms are more delocalized in HEO, indicating stronger interactions between TM and O. Moreover, the weak hybridization phenomenon in Li/Zn–O ionic bonds and unique Li/Zn–O–TM bridge-type charge-transfer structures observed in HEO, align with the findings reported in previous literature.[16,36] As illustrated in Fig. S12 and S13 (SI), the local coordination environment constructed by the strong-bond-forming ions (Ti, Cu, and F) anchored within the TM layer plays a pivotal role in enhancing the overall covalency of the material system. These results demonstrate that the cation–anion dual-site high-entropy doping strategy effectively modulates the local covalency of the material, thereby enhancing its structural stability and ultimately achieving excellent sodium storage performance.[20]

To validate the superiority of the cation–anion dual-site high-entropy doping strategy, we evaluated the sodium storage performance of NFM and HEO using half-cells. As shown in Fig. 3a, the cyclic voltammetry (CV) curves of the two materials exhibit significant differences. On the one hand, NFM shows redox peaks at approximately 3.4 V due to Na^+/vacancy ordering, a process that reduces structural stability and hinders Na^+ diffusion, whereas this phenomenon is absent in HEO.[30] On the other hand, in the high-voltage range of 4.0–4.2 V, NFM presents sharp and asymmetric redox peaks, in stark contrast to the smooth and symmetric peaks of HEO. This demonstrates that HEO effectively suppresses Na^+/vacancy ordering, as well as severe phase transitions and irreversible oxygen reactions at high voltages. The galvanostatic charge/discharge curves in Fig. 3b further validate the positive role of the cation–anion dual-site high-entropy doping strategy in suppressing irreversible phase transitions and limiting oxygen redox reactions. In addition, HEO shows an acceptable reversible capacity of 152.27 mA h g^{-1} with higher initial Coulombic efficiency of 98.71%. As shown in Fig. 3c, d and S14 (SI), HEO demonstrates superior rate performance compared to NFM, with reversible capacities of 150.18, 145.64, 141.21, 126.75, 115.98, and 98.01 mA h g^{-1} at 0.2, 0.5, 1.0, 5.0, 10.0, and 20.0C, respectively. HEO exhibits a medium voltage of 3.205 V, energy density of 482.3 Wh kg^{-1} and power density of 100.69 W kg^{-1} at 0.2C (Fig. S15, SI). Even at a high current density of 20.0C, its performance remains outstanding, achieving 2.707 V, 268.1 Wh kg^{-1}, and 8.94 kW kg^{-1}, respectively. Meanwhile, HEO demonstrates excellent long-term cycling stability and delivers a high capacity retention of 73.69% with a reversible capacity of 95.57 mA h g^{-1} after 500 cycles at 10.0C (Fig. 3e). In contrast, NFM exhibits significant capacity degradation, and the battery fails completely after 150 cycles. It is noteworthy that the cycling stability of HEO is comprehensively superior to that of NFM at various current densities and cut-off voltages (Fig. S16–S20, SI).

Subsequently, we further investigated the effect of the cation–anion dual-site high-entropy doping strategy on the temperature tolerance of O3-type layered oxide cathode materials. As the operating temperature decreased (−20 °C), the reversible capacities of both electrode materials declined, and HEO exhibits significantly higher capacity retention than NFM

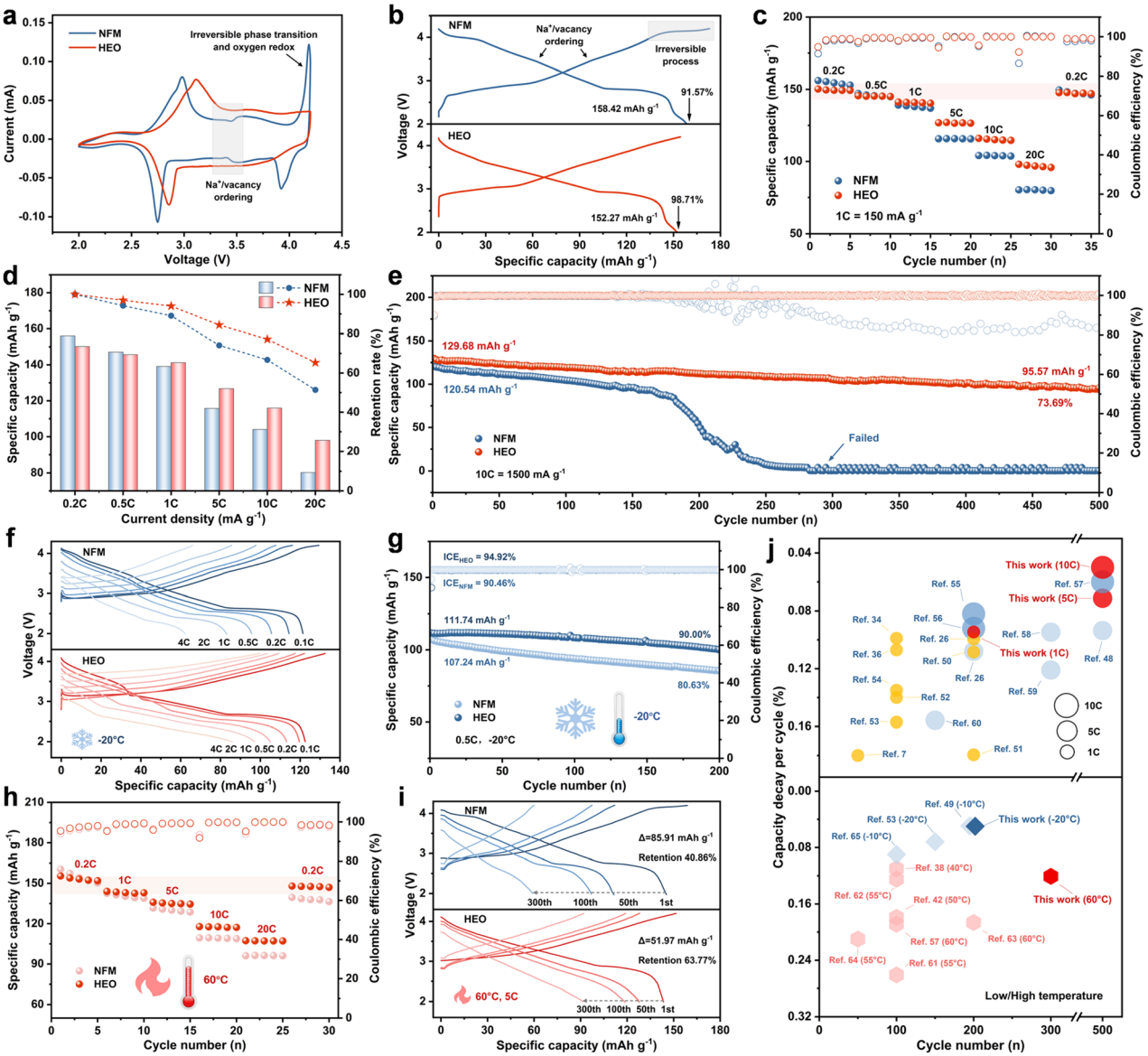

Fig. 3 (a) CV curves of NFM and HEO at 0.1 mV s^{-1} for the first cycle. (b) Initial galvanostatic charge/discharge curves of NFM and HEO at 0.1C (1C = 150 mA g^{-1}). (c) Rate performance of NFM and HEO. (d) Specific capacity comparison between NFM and HEO at different current densities. (e) Long-term cycling performance at 10.0C. (f) Rate performance and (g) cycling performance at −20 °C (low temperature). (h) Rate performance and (i) cycling performance at 60 °C (high temperature). (j) Comparison of half-cell performance with reported literature over the past three years.[7,26,34,36,38,44,50–67]

(75.16% *vs.* 69.28%, Fig. S21, SI). As shown in Fig. 3f, g, and S22 (SI), HEO demonstrated superior rate performance and cycling stability compared to NFM, delivering a high reversible capacity of 85.90 mA h g^{-1} at 4.0C and a high capacity retention of 90% after 200 cycles. When the operating temperature was raised to 60 °C, NFM suffered from severe side reactions, leading to poor sodium storage performance (Fig. 3h, i, and S23–S24, SI).[51] In contrast, HEO exhibited excellent rate performance (107.30 mA h g^{-1} at 20.0 C) and outstanding cycling stability (capacity retention of 63.77% after 300 cycles). Compared with advanced O3-type layered oxide cathodes reported in the past three years, the HEO developed in this work achieves a balance among reversible capacity, cycling stability, rate performance, and temperature tolerance. Its comprehensive electrochemical performance significantly surpasses that of previously reported counterparts (Fig. 3j, S25, and Tables S6–S7, SI).

To elucidate the origin of the enhanced electrochemical performance, we first systematically investigated the charge transfer kinetics. Based on the linear fitting results between the square root of the scanning rate ($v^{1/2}$) and the corresponding peak current, the Na^+ diffusion kinetics of HEO are significantly improved compared to those of NFM (Fig. S26, SI). This conclusion was further validated by the galvanostatic intermittent titration technique (GITT) analysis: HEO exhibits a higher average Na^+ diffusion coefficient during the charge/discharge process, especially within the high-voltage range of 4.0–4.2 V

(Fig. S27, SI). Meanwhile, the more continuous and smaller variations in the Na^+ diffusion coefficient indirectly reflect the milder phase transitions in HEO. Moreover, electrochemical impedance spectroscopy (EIS) results show that the impedance values of HEO during the cycling process are also lower than those of NFM, indicating fast charge transfer in HEO (Fig. S28, SI). These findings collectively highlight the positive role of the cation–anion dual-site high-entropy doping strategy in enhancing the electrochemical reaction kinetics, which is responsible for the improved rate performance.

In-situ X-ray diffraction (XRD) is employed to monitor the structural evolution of NFM and HEO during the initial charge/discharge process (Fig. 4a, b and S29–S30, SI). During the initial charge process, both NFM and HEO show consistent variations in their characteristic diffraction peaks. As Na^+ extraction enhances the interlayer O^{2-}–O^{2-} electrostatic repulsion and leads to *c*-axis expansion, the $(003)_{O3}$ peaks shift toward lower angles. Concurrently, the shifts of the $(101)_{O3}$ and $(012)_{O3}$ peaks toward higher angles correspond to contraction of the *ab*-plane, which is attributed to the progressive oxidation of active transition metal ions. Subsequently, an O′3 phase (monoclinic, *C*2/*m*) distinct from the O3 phase is observed in NFM. This phase is typically associated with collective Jahn–Teller distortion of Ni^{3+}, which exacerbates lattice distortion and compromises structural stability.[36,41,49] Noticeably, HEO in the same stage maintains a solid solution reaction of the O3 phase. The absence of the O′3 phase indicates that Jahn–Teller distortion is effectively mitigated, benefiting from the expanded TMO_2 slabs and a robust TM–O bonding environment.[30,68] Subsequently, the appearance of the $(003)_{P3}$ peaks in NFM and HEO confirms the phase transformation to the P3 phase, with the solid solution reactions (accompanied by minor variations in unit cell parameters) proceeding continuously. When the voltage exceeds 4.0 V, NFM and HEO undergo distinct phase transitions: NFM rapidly transforms from the P3 phase to the Na-deficient O3′ phase (hexagonal, similar to the pristine O3

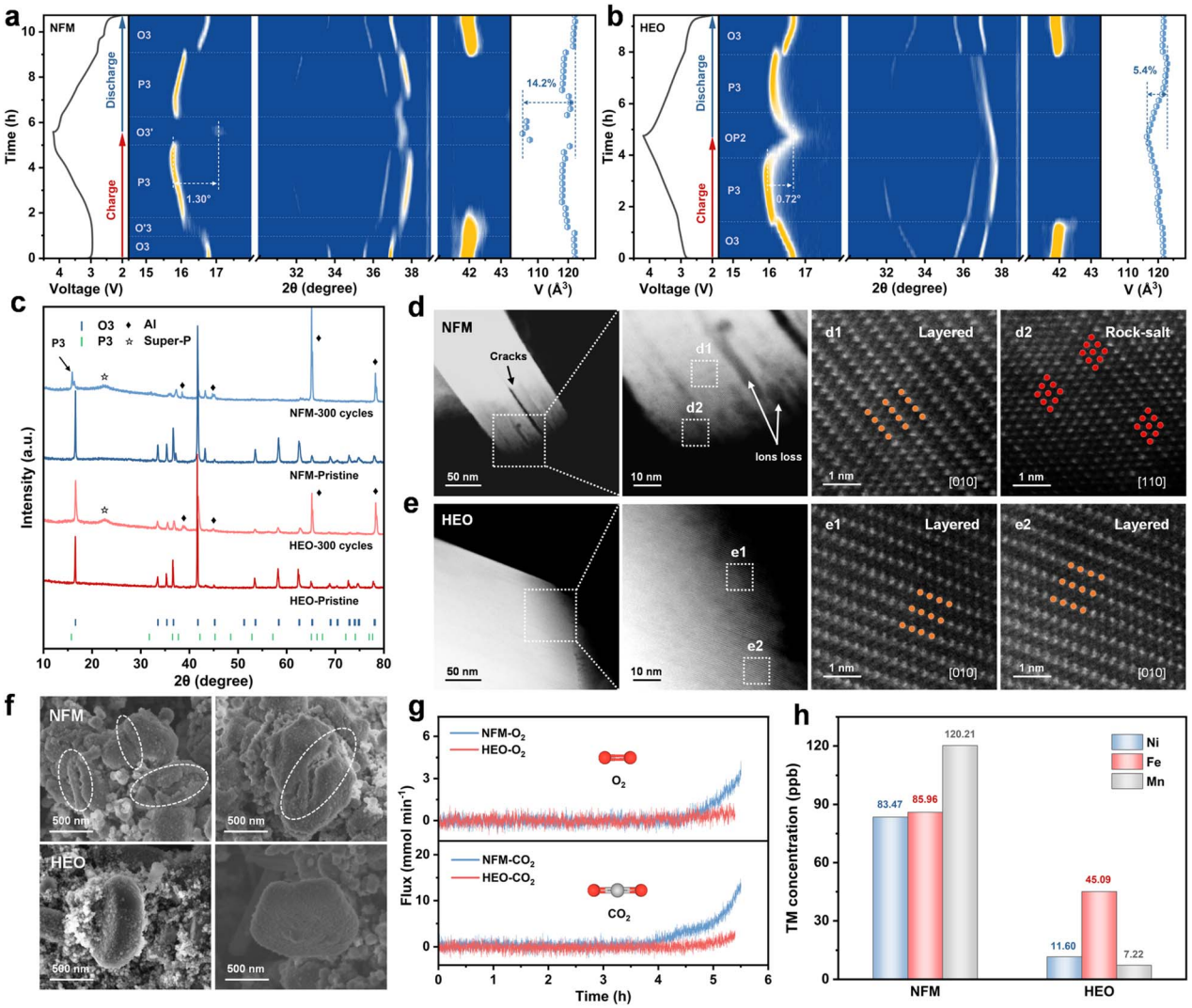

Fig. 4 *In-situ* XRD contour maps and the corresponding lattice volume changes of (a) NFM and (b) HEO during the first cycle at 0.2C. (c) XRD patterns before and after 300 cycles. (d and e) AC-HAADF-STEM images and (f) SEM images of NFM and HEO after 300 cycles. (g) Comparison of *in-situ* DEMS results for the first charge to 4.2 V. (h) Concentrations of deposited transition metal ions in NFM||Na and HEO||Na after 300 cycles.

structure), which induces severe lattice distortion and a propensity for irreversible lattice oxygen loss and transition metal ion dissolution.[7] In contrast, HEO undergoes a gradual evolution into the highly reversible OP2 phase.[41,69] Lattice parameters and volume changes during the initial charge/discharge cycle were further obtained from *in-situ* XRD pattern Rietveld refinement (Fig. S31, SI). NFM exhibits an abrupt 14.2% maximum volume change, triggering stress concentration and crack propagation, while HEO undergoes a gentle 5.4% variation to maintain particle integrity. In summary, the anchored TM layer constructed by the cation–anion dual-site high-entropy doping strategy enables a highly reversible O3 → P3 → OP2 phase transition. It efficiently suppresses Jahn–Teller distortion and the unfavorable O3′ phase, thereby significantly improving cycling stability (Fig. S32, SI).

The effect of the cation–anion dual-site high-entropy doping strategy on structural stability during long-term cycling is further revealed by XRD, SEM, TEM, and AC-STEM. As illustrated in Fig. 4c and S33 (SI), NFM exhibits residual P3 phase peaks after 300 cycles, indicative of irreversible phase transitions within the material. In sharp contrast, HEO retains a pure O3 phase structure, testifying to its exceptional structural stability that underpins enhanced cycling longevity. Subsequently, atomic-resolution AC-HAADF-STEM images in Fig. 4d and e reveal the detailed structural information of the cathode materials after cycling. Specifically, the HEO cathode preserves a well-defined layered architecture, free of discernible cracking or substantial phase transformations. Evidently, the maximal retention of the pristine structure constitutes the critical structural basis for the long-term cycling stability of HEO.[69] However, the NFM cathode suffers from prominent cracking, with extensive rock-salt phase formation at the fracture sites; meanwhile, severe surface reconstruction synergistically undermines its structural integrity.[13,70] As observed from the SEM and TEM images, the surfaces of NFM particles are covered with numerous cracks, accompanied by severe particle fragmentation (Fig. 4f and S34, SI). In stark contrast, the HEO particles retain their structural integrity after cycling.[12] Furthermore, TEM images clearly demonstrate that a uniform and dense cathode electrolyte interphase (CEI) layer is formed on the surface of HEO. This interfacial layer effectively suppresses the interfacial side reactions and the transition metal ion dissolution, thereby significantly enhancing the sodium storage performance of HEO. The real-time release behavior of O_2 ($m/z = 32$) and CO_2 ($m/z = 44$) during the initial charge process is probed by *in-situ* differential electrochemical mass spectrometry (DEMS, Fig. 4g).[71] Compared to NFM, HEO exhibits significant reduction in the release of O_2 and CO_2 during the process, demonstrating that irreversible O_2 release and interfacial side reactions are effectively suppressed. Additionally, inductively coupled plasma optical emission spectrometry (ICP-OES) measurements reveal that the dissolution of Ni, Fe, and Mn from HEO is significantly lower than that from NFM (Fig. 4h).[41] This observation indicates that the robust TM–O bonds exhibit excellent stability during the charge/discharge process, which effectively suppresses transition metal ion dissolution, preserves active redox sites, and mitigates structural degradation. Collectively, these findings underscore the favorable effect of the cation–anion dual-site high-entropy doping strategy on reinforcing the covalency of TM–O bonds, a key contributor to the enhanced cycling performance.

Ex-situ X-ray photoelectron spectroscopy (XPS) and X-ray absorption spectroscopy (XAS) are employed to elucidate the charge compensation mechanisms in NFM and HEO. The Ni 2p and Fe 2p XPS spectra of the two materials exhibit similar peak shifts during the charge/discharge process (Fig. 5a–c and S35, SI). As electrochemically active elements, Ni and Fe contribute to the capacity *via* electron transfer and valence state variations, following the redox pathways of $Ni^{2+} \rightarrow Ni^{4+}$ and $Fe^{3+} \rightarrow Fe^{4+}$. In contrast, no significant peak shifts were observed for Mn in NFM, nor for Mn, Li, Ti, Cu, and Zn in HEO in the XPS spectra, indicating that these elements act as electrochemically inert species to stabilize the host structure (Fig. S36, SI). Upon charging to 4.2 V, a new characteristic peak at approximately 530.5 eV (assigned to $(O_2)^{n-}$ species) emerged in the O 1s XPS spectra of both materials (Fig. 5d). Notably, the signal intensity in NFM was distinctly higher than that in HEO, which is consistent with the electron paramagnetic resonance (EPR) measurements, indicating that more pronounced oxygen redox reactions occurred in NFM (Fig. S37, SI).[21,34,38] Furthermore, obvious disparities between the two materials were observed after discharging to 2.0 V: the characteristic peak of $(O_2)^{n-}$ species almost completely vanished in HEO, testifying to the highly reversible nature of its oxygen redox reactions; by contrast, partial $(O_2)^{n-}$ species was detected in NFM, revealing the poor reversibility of oxygen redox reactions.[64,72] This phenomenon is further confirmed by the Raman spectroscopy results (Fig. S38, SI).[41,73] These results demonstrate the superior lattice oxygen stability and controllable redox activity of HEO, which in turn ensure excellent structural stability throughout charge/discharge cycling. Normalized X-ray absorption near-edge structure (XANES) spectra of the Ni, Fe, and Mn K-edges are shown in Fig. 5e–g and S39 (SI). For both NFM and HEO, the Ni and Fe K-edge XANES spectra exhibited pronounced shifts during charging and reversibly reverted to their initial positions upon discharging, further demonstrating the key role of Ni and Fe as electrochemically active elements in the charge compensation mechanism.[36] Meanwhile, Mn retained a consistent +4 oxidation state throughout the process, with negligible shifts in its K-edge XANES profile, thus further verifying its electrochemical inertness as a structural framework component.[71] Fourier-transformed extended X-ray absorption fine structure (FT-EXAFS) spectra of the two materials in different states offer profound insights into the evolution of local structures during the charge/discharge process (Fig. 5h–j and S40–S41, SI). The first coordination shell corresponds to Ni/Fe/Mn–O bonds. During charging, the Ni/Fe–O bond length shortens markedly, accompanied by continuous contraction of the TMO_6 octahedral structure, a phenomenon closely correlated with the progressive oxidation of the electrochemically active Ni/Fe sites. In contrast, the negligible shifts in the Mn–O bond signals confirm the stable +4 oxidation state of Mn throughout the process.[34,65,71]

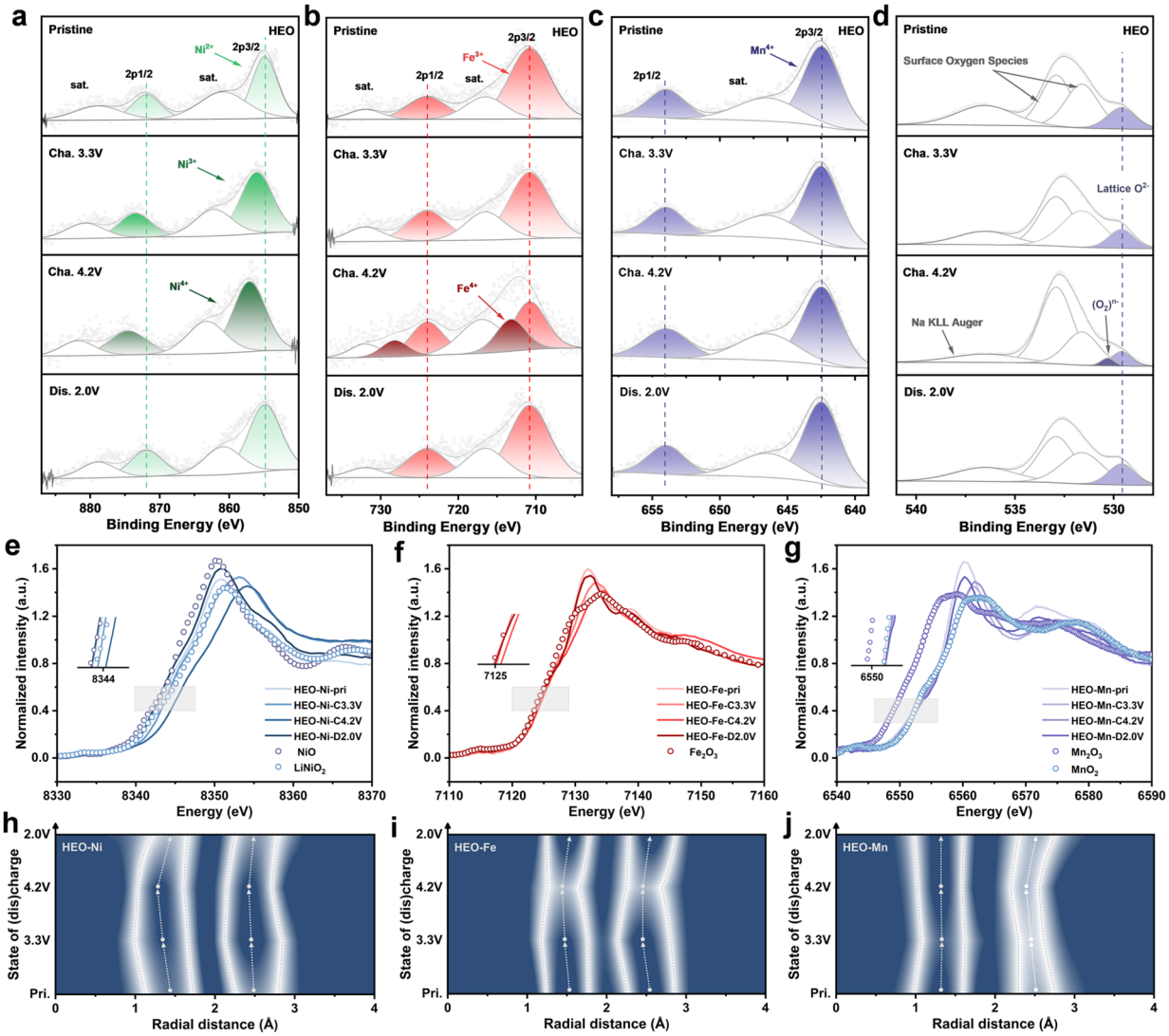

Fig. 5 XPS spectra of (a) Ni 2p, (b) Fe 2p, (c) Mn 2p, and (d) O 1s in HEO at various charge/discharge states during the initial cycle. XANES spectra of (e) Ni-K-edge, (f) Fe K-edge, and (g) Mn K-edge of HEO. Contour maps of (h) Ni, (i) Fe, and (j) Mn K-edge FT-EXAFS spectra of HEO.

The air stability and full-cell performance of O3-type layered oxide cathode materials exert a decisive influence on their prospects for commercial application.[4,27] The phase structure evolution of NFM and HEO powders upon prolonged exposure to ambient air with a relative humidity of about 70% was first investigated by XRD (Fig. 6a and b). After 7 days of air exposure, characteristic diffraction peaks corresponding to $Na_2CO_3 \cdot nH_2O$, the monoclinic O3 phase, and the hydration phase emerged in NFM, indicating that Na^+ continuously leaches out, accompanied by structural distortion and further H_2O insertion.[74] When the air exposure duration extends to 10 days, the characteristic peaks of the undesired byproducts become more pronounced. Meanwhile, the $(003)_{O3}$ diffraction peak exhibits a significant shift relative to the pristine sample, signifying substantial alterations in the interlayer spacing of the layered structure. In stark contrast, HEO with regulated local chemistry retains a highly crystalline structure, with negligible shifts in its characteristic peaks even after 10 days of exposure to such high-humidity air (Fig. S42, SI).[57] In addition, HEO also exhibits minimal capacity degradation, excellent rate performance, and remarkable cycling stability after prolonged air exposure (Fig. 6c–e, S43 and S44, SI). These observations explicitly verify that the enhanced local covalency of the material, imparted by the cation–anion dual-site high-entropy doping strategy, can effectively elevate the air stability of O3-type layered oxide cathode materials. Subsequently, full cells were assembled using hard carbon anodes to systematically evaluate the electrochemical performance of HEO (Fig. 6f and g). As illustrated in Fig. 6h and S45 (SI), the HEO‖HC full cell displays excellent rate performance, delivering high reversible capacities of 138.31, 124.11, 114.58, 107.28, and 99.93 mA h g^{-1} at current densities of 10, 20, 50, 100, and 200 A g^{-1}, respectively. At a current density of 50 mA g^{-1}, the HEO‖HC full cell achieves a favorable energy density of 252.35 Wh kg^{-1}, calculated based on the combined mass of the cathode and anode. More importantly, the HEO‖HC full cell demonstrates outstanding

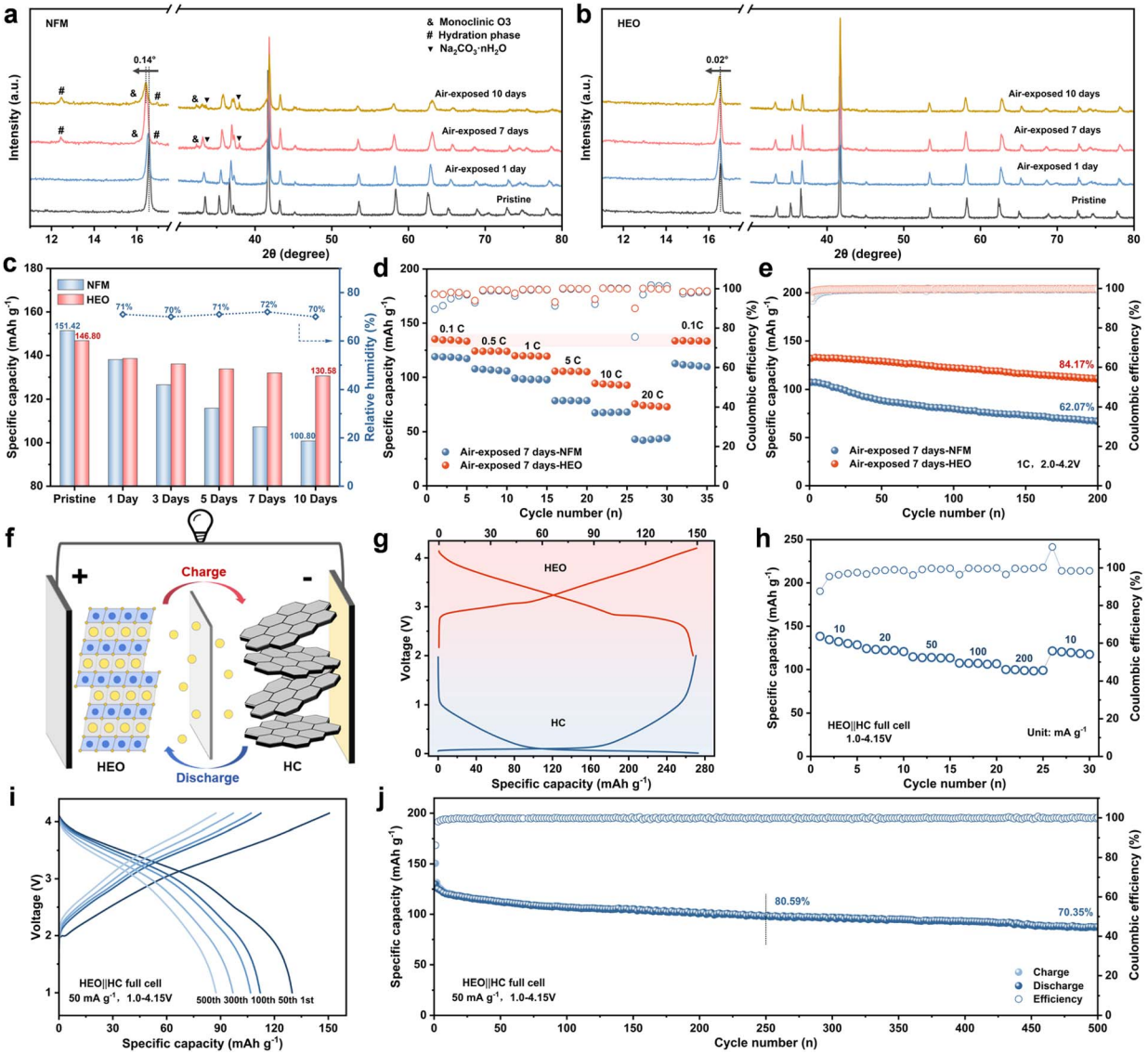

Fig. 6 XRD patterns of (a) NFM and (b) HEO before and after air exposure. Comparison of (c) specific capacity, (d) rate performance, and (e) cycling performance of NFM and HEO exposed to air. (f) Schematic diagram of the HEO||HC full cell. (g) Initial galvanostatic charge/discharge curves of the HEO cathode and HC anode after precycling. (h) Rate performance and (i and j) long-term cycling performance of the HEO||HC full cell.

cycling stability, exhibiting a high capacity retention of 70.35% after 500 cycles (Fig. 6i and j). Moreover, the HEO||HC full cells exhibit high discharge capacity and excellent cycling stability over a wide voltage range (Fig. S46, SI). These results demonstrate that HEO with regulated local chemistry exhibits considerable potential for practical applications.

Conclusions

In summary, this work proposes a cation–anion dual-site high-entropy doping strategy to modulate the local chemical environment of O3-type layered oxide cathode materials, thereby achieving a remarkable enhancement in their sodium storage performance. Specifically, the introduction of Li, Ti, Cu and Zn at cation sites, combined with F doping at anion sites, synergistically strengthens the covalency of the TM–O bonds. This dual-site synergistic modulation effect exhibits prominent advantages: (i) the strongly covalent TM–O bonds can effectively suppress the undesirable phase transitions during the charge/discharge process, thus preserving the integrity of the electrode material; (ii) it significantly inhibits the occurrence of irreversible oxygen redox reactions, reduces oxygen loss, and simultaneously mitigates the dissolution of transition metal ions, fundamentally improving the long-term cycling stability of the material. As a result, the designed HEO not only delivers a high specific capacity of 152.27 mA h g^{-1}, but also achieves an excellent capacity retention of 73.69% after 500 cycles. More importantly, this material also possesses outstanding temperature tolerance, favorable air stability and reliable full-cell performance, highlighting its enormous application potential

in the practical implementation of SIBs. The cation–anion dual-site high-entropy doping strategy developed in this work features excellent universality and scalability and provides an efficient approach for regulating the local chemical environment of O3-type layered oxide cathodes. Moreover, the simultaneous doping at both TM and O sites enriches the design theory of high-entropy cathode materials for advanced sodium-ion batteries.

Author contributions

L. L., K. L., and S. Z. obtained the funds and supervised the project; T. H. and K. L. conceived the idea; T. H., Q. Y., and G. Y. designed the experiments; T. H., Q. Y., G. Y., M. L., X. B., T. L., X. Z., and J. X. performed experiments; T. H., K. L., X. Z., and X. T. analyzed the data; and T. H. wrote the original manuscript. All authors revised and approved the manuscript.

Conflicts of interest

There are no conflicts to declare.

Data availability

The data supporting the findings of this study are available within the article or its supplementary information (SI). Supplementary information is available. See DOI: https://doi.org/10.1039/d6sc01783e.

Acknowledgements

This work was funded by the National Natural Science Foundation of China (52202286 and 22309002), Key Research and Development Program of Zhejiang Province (2024C01057), Natural Science Foundation of Hebei Province (E2024202239 and B2024202081), Science and Technology Plan Project of Wenzhou Municipality (ZG2024055), Science Research Project of Hebei Education Department (CXY2024036), the Tianjin Science and Technology Plan Project (24JCQNJC00750), and China National Postdoctoral Program for Innovative Talents (BX20250118). We would like to thank the Advanced Materials Testing and Analysis Center of Hebei University of Technology. The authors extend their gratitude to Scientific Compass (https://www.shiyanjia.com) for providing invaluable assistance with EPR.

Notes and references

1 Q. Liu, Z. Hu, W. Li, C. Zou, H. Jin, S. Wang, S. Chou and S. Dou, *Energy Environ. Sci.*, 2021, **14**, 158–179.
2 J. Ren, H. Zhu, Y. Fang, W. Li, S. Lan, S. Wei, Z. Yin, Y. Tang, Y. Ren and Q. Liu, *Carbon Neutralization*, 2023, **2**, 339–377.
3 H. Kim and J. Kim, *eScience*, 2024, **4**, 100232.
4 F. Li, W. Tang, J. Wu, L. Zhang, A. Mu and Z. Chen, *Adv. Energy Mater.*, 2024, **14**, 2401564.
5 Y. Gao, H. Zhang, J. Peng, L. Li, Y. Xiao, L. Li, Y. Liu, Y. Qiao and S. Chou, *Carbon Energy*, 2024, **6**, e464.
6 Z. Chen, Y. Deng, J. Kong, W. Fu, C. Liu, T. Jin and L. Jiao, *Adv. Mater.*, 2024, **36**, 2402008.
7 N. Hong, J. Li, H. Wang, X. Hu, B. Zhao, F. Hua, Y. Mei, J. Huang, B. Zhang, W. Jian, J. Gao, Y. Tian, X. Shi, W. Deng, G. Zou, H. Hou, Z. Hu, Z. Long and X. Ji, *Adv. Funct. Mater.*, 2024, **34**, 2402398.
8 X. Zhang, Q. Yang, J. Xu, T. Lv, M. Li, G. Yu, T. Huo, X. Zhou, X. Bai, L. Li and K. Lei, *Chin. Chem. Lett.*, 2025, 112268.
9 D. Eum, B. Kim, J. Song, H. Park, H. Jang, S. Kim, S. Cho, M. Lee, J. Heo, J. Park, Y. Ko, S. Park, J. Kim, K. Oh, D. Kim, S. Kang and K. Kang, *Nat. Mater.*, 2022, **21**, 664–672.
10 S. Thekkekara, P. Tripathi, J. Sudharma, P. Anurag, V. Srihari, H. Poswal, A. Singh and M. Shaijumon, *Small*, 2025, **21**, 2502341.
11 M. Gu, J. Xu, X. Shi, L. Shao and Z. Sun, *Battery Energy*, 2024, **3**, 20230046.
12 Y. Bi, J. Tao, Y. Wu, L. Li, Y. Xu, E. Hu, B. Wu, J. Hu, C. Wang, J. Zhang, Y. Qi and J. Xiao, *Science*, 2020, **370**, 1313–1317.
13 J. Li, H. Yang, Q. Deng, W. Li, Q. Zhang, Z. Zhang, Y. Chu and C. Yang, *Angew. Chem., Int. Ed.*, 2024, **63**, e202318042.
14 J. Wu, W. Zhou, S. Zhang, J. Wang, J. Dong, C. Ma, K. Zhang, Y. Lu, Z. Yan, M. Song and J. Chen, *Angew. Chem., Int. Ed.*, 2025, **64**, e202519551.
15 X. Ou, T. Liu, W. Zhong, X. Fan, X. Guo, X. Huang, L. Cao, J. Hu, B. Zhang, Y. Chu, G. Hu, Z. Lin, M. Dahbi, J. Alami, K. Amine, C. Yang and J. Lu, *Nat. Commun.*, 2022, **13**, 2319.
16 Z. Wang, R. Hu, H. Chen, Y. Ye, Q. Zhao, Z. Du and S. Yang, *Energy Environ. Sci.*, 2025, **18**, 6832–6840.
17 Y. Sun, J. Weng, P. Zhou, W. Yuan, Y. Pan, X. Wu, J. Zhou and F. Cheng, *Adv. Mater.*, 2024, **36**, 2410575.
18 M. Sun, Z. Liu, L. Liu, Y. Zheng, S. Lv, N. Zhang, L. Deng, L. Zhao and Z. Wang, *Adv. Energy Mater.*, 2025, **15**, e03154.
19 X. Cai, Z. Shadike, N. Wang, X. Li, Y. Wang, Q. Zheng, Y. Zhang, W. Lin, L. Li, L. Chen, S. Shen, E. Hu, Y. Zhou and J. Zhang, *J. Am. Chem. Soc.*, 2025, **147**, 5860–5870.
20 Q. Lai, H. Yue, D. Yang, G. Gao, H. Chen, X. Gao, Z. Liu, Q. Gu and W. Luo, *Adv. Energy Mater.*, 2025, **16**, e04890.
21 H. Lu, S. Chu, J. Tian, Q. Wang, C. Sheng, C. Cheng, R. Liu, A. D'Angelo, W. K. Pang, L. Zhang, H. Zhou and S. Guo, *Adv. Funct. Mater.*, 2024, **34**, 2305470.
22 Q. Lai, C. Liu, D. Yang, X. Gao, R. Yang, Q. Li, Z. Liu, Q. Gu and W. Luo, *Adv. Funct. Mater.*, 2025, **36**, e16173.
23 C. Cheng, Y. Shen, C. Chen, S. Tang, Z. Zhuo, Q. Niu, C. Yuan, T. Chen, L. Wang, J. Guo, D. Sun and L. Zhang, *Adv. Energy Mater.*, 2025, **15**, e04261.
24 E. Gabriel, C. Ma, K. Graff, A. Conrado, D. Hou and H. Xiong, *eScience*, 2023, **3**, 100139.
25 H. Wang, L. Li, W. Han, H. Guo, A. BobrikovIvan, Y. Chai and X. Liu, *Renewables*, 2023, **1**, 253–265.
26 J. Yao, X. Wang, P. Hu, J. Fan, X. Yang, W. Jiang, S. Jiang, P. Dong, Y. Zhang, J. Duan and Z. Zhou, *Adv. Funct. Mater.*, 2024, 2419967.
27 L. Duan, Y. Zhang, H. Tang, J. Liao, G. Zhou and X. Zhou, *Adv. Mater.*, 2025, **37**, 2411426.
28 L. He, T. Feng, Q. Wu, Y. Cao and F. Song, *Rare Met.*, 2025, **44**, 5355–5369.

29 K. Zhang, Z. Xu, G. Li, R. Luo, C. Ma, Y. Wang, Y. Zhou and Y. Xia, *Adv. Energy Mater.*, 2023, **13**, 2302793.
30 F. Ding, C. Zhao, D. Xiao, X. Rong, H. Wang, Y. Li, Y. Yang, Y. Lu and Y. Hu, *J. Am. Chem. Soc.*, 2022, **144**, 8286–8295.
31 B. Wang, J. Ma, K. Wang, D. Wang, G. Xu, X. Wang, Z. Hu, C. Pao, J. Chen, L. Du, X. Du and G. Cui, *Adv. Energy Mater.*, 2024, **14**, 2470094.
32 Z. Li, W. Xi, Z. Jiang, Y. Zhang, R. Wang, Y. Gong, H. Wang and J. Jin, *Small*, 2025, **21**, e06854.
33 H. Ren, Q. Zhou, Y. Li, L. Zheng, Q. Ni, Q. Li, J. Qian, S. Li, Y. Zhao, F. Wu, C. Wu and Y. Bai, *Energy Storage Mater.*, 2025, **76**, 104095.
34 H. Wang, J. Gao, Y. Mei, L. Ni, Y. He, N. Hong, J. Huang, W. Deng, G. Zou, H. Hou, T. Liu, C. Liang, X. Ji and K. Amine, *Angew. Chem., Int. Ed.*, 2025, **64**, e202418605.
35 Y. Wang, X. Zhao, J. Jin, Q. Shen, Y. Hu, X. Song, H. Li, X. Qu, L. Jiao and Y. Liu, *J. Am. Chem. Soc.*, 2023, **145**, 22708–22719.
36 T. Zhang, M. Ren, Y. Huang, F. Li, W. Hua, S. Indris and F. Li, *Angew. Chem., Int. Ed.*, 2024, **63**, e202316949.
37 X. Jia, Q. Peng, Y. Liu, D. Chen, J. Wang, J. Li, Y. Zhu, N. Xu, L. Kong, H. Liu, G. Zhang, Z. Jian, C. Cheng, H. Dong, L. Zhang, Y. Sun, S. Chen, X. Guo, S. Dou and Y. Xiao, *Nat. Commun.*, 2025, **16**, 10477.
38 X. Wang, H. Li, Z. Dai, J. Li, Y. Song, B. Han, X. Wang, J. Chen, C. Dong, Z. Mao and L. Zhang, *Energy Storage Mater.*, 2025, **79**, 104345.
39 D. Yang, C. Liu, X. Gao, Z. Zhao, Q. Gu, Y. Long, Q. Lai, H. Chen, Z. Liu and W. Luo, *Angew. Chem., Int. Ed.*, 2025, **64**, e202500939.
40 G. Liu, W. Xu, J. Wu, Y. Li, L. Chen, S. Li, Q. Ren and J. Wang, *J. Energy Chem.*, 2023, **83**, 53–61.
41 Q. Huang, D. Cheng, B. Wu, Z. Liu, K. Zhang, Y. Zou, L. Li and Y. Chen, *Adv. Funct. Mater.*, 2025, **36**, e18419.
42 L. He, F. Song, Y. Cao and Q. Chen, *Energy Storage Mater.*, 2025, **80**, 104370.
43 Y. Dong, Z. Zhou, Y. Ma, H. Zhang, F. Meng, Y. Wu and Y. Ma, *ACS Energy Lett.*, 2024, **9**, 5096–5119.
44 K. Zhang, J. Zou, Z. Xu, G. Liu, L. He, Q. Yu, F. Wang and Y. Xia, *J. Am. Chem. Soc.*, 2025, **147**, 48147–48157.
45 W. Lai, F. Luo, L. Zeng, Z. Lai, K. Jia, F. Xiao, L. Chen, Y. Lu, Q. Qian, Q. Chen, K. Zhang, Z. Yan and J. Chen, *Adv. Funct. Mater.*, 2025, **36**, e17602.
46 J. Huang, Z. Xue, S. Lee, H. Chen, X. Ji and K. Du, *J. Am. Chem. Soc.*, 2025, **147**, 22444–22452.
47 X. Zhang, Y. Qiao, S. Guo, K. Jiang, S. Xu, H. Xu, P. Wang, P. He and H. Zhou, *Adv. Mater.*, 2019, **31**, 1807770.
48 Y. Huang, F. Zhang, X. Xu, Y. Wang, P. Sun, K. Jing, F. Wu, Z. An, X. Han, Y. Cao, Y. Liu, X. Liao, Y. Li, Z. Xu and Z. Lu, *Energy Storage Mater.*, 2025, **83**, 104641.
49 S. Gao, Z. Zhu, H. Fang, K. Feng, J. Zhong, M. Hou, Y. Guo, F. Li, W. Zhang, Z. Ma and F. Li, *Adv. Mater.*, 2024, **36**, 2311523.
50 X. Zhang, F. Xie, J. Han, X. Wang, T. Liu, J. Yu and L. Zhang, *Small*, 2025, **21**, 2502292.
51 X. Liang, X. Song, H. H. Sun, H. Kim, M. Kim and Y. Sun, *Nat. Commun.*, 2025, **16**, 3505.
52 H. Bi, X. Sun, B. Zhao, R. Li, Y. Zhang, X. Wang, M. Zhang, D. Luo and Z. Chen, *Adv. Energy Mater.*, 2025, **15**, 2501229.
53 L. Zhang, Y. Hong, J. Xu, S. Lin, Z. Lin, L. Zheng, H. Yao and Z. Hong, *Energy Storage Mater.*, 2025, **82**, 104556.
54 F. Ding, P. Ji, Z. Han, X. Hou, Y. Yang, Z. Hu, Y. Niu, Y. Liu, J. Zhang, X. Rong, Y. Lu, H. Mao, D. Su, L. Chen and Y. Hu, *Nat. Energy*, 2024, **9**, 1529–1539.
55 T. Yuan, P. Li, Y. Sun, H. Che, Q. Zheng, Y. Zhang, S. Huang, J. Qiu, Y. Pang, J. Yang, Z. Ma and S. Zheng, *Adv. Funct. Mater.*, 2025, **35**, 2414627.
56 C. Cai, X. Li, J. Li, R. Yu, P. Hu, T. Zhu, T. Li, S. Lee, N. Xu, H. Fan, J. Wu, L. Zhou, L. Mai and K. Amine, *Nat. Commun.*, 2025, **16**, 100.
57 X. Yuan, Y. Guo, L. Gan, X. Yang, W. He, X. Zhang, Y. Yin, S. Xin, H. Yao, Z. Huang and Y. Guo, *Adv. Funct. Mater.*, 2022, **32**, 2111466.
58 L. Yu, Y. Chang, M. Liu, Y. Feng, D. Si, X. Zhu, X. Wang, P. Wang and S. Xu, *ACS Appl. Mater. Interfaces*, 2023, **15**, 23236–23245.
59 Z. Song, S. Kansara, S. Cheng, M. Yang, F. Li, C. Qi, S. Li, J. Hwang and Y. Bai, *ACS Energy Lett.*, 2025, **10**, 5199–5208.
60 H. Wang, H. Chen, Y. Mei, J. Gao, L. Ni, N. Hong, B. Zhang, F. Zhu, J. Huang, K. Wang, W. Deng, D. Silvester, C. Banks, S. Yasar, B. Song, G. Zou, H. Hou and X. Ji, *ACS Nano*, 2024, **18**, 13150–13163.
61 L. Yao, P. Zou, C. Wang, J. Jiang, L. Ma, S. Tan, K. Beyer, F. Xu, E. Hu and H. Xin, *Adv. Energy Mater.*, 2022, **12**, 2201989.
62 J. Wang, F. Xu, X. Fan, C. Zheng, Y. Zhao, L. Zuo, X. Yun, D. Lu, P. Xiao and Y. Chen, *Chem. Eng. J.*, 2024, **500**, 157032.
63 Y. Wu, H. Hu, J. Li, H. Dong, Y. Zhu, S. Chen, N. Wang, J. Wang and Y. Xiao, *Chem. Sci.*, 2025, **16**, 3928–3937.
64 J. Kuang, Z. Liu, L. Fu, Y. Shi, M. Zhang, Y. Wang, N. Ding, D. Sun, Y. Tang and H. Wang, *Angew. Chem., Int. Ed.*, 2025, **64**, e202500715.
65 W. Xu, C. Cheng, L. Wang, T. Chen, Z. Zhou, T. Yan, S. Shen, P. Zeng and L. Zhang, *Adv. Energy Mater.*, 2026, **16**, e04557.
66 H. Hu, M. Yang, D. Chen, N. Xu, J. Li, Y. Zhu, Y. Wu, H. Dong, J. Wang, C. Yao, Y. Yan, S. Chen, N. Wang, W. K. Pang, Y. Sun, J. Wang and Y. Xiao, *Angew. Chem., Int. Ed.*, 2026, **65**, e19108.
67 T. Yuan, S. Li, Y. Sun, J. Wang, A. Chen, Q. Zheng, Y. Zhang, L. Chen, G. Nam, H. Che, J. Yang, S. Zheng, Z. Ma and M. Liu, *ACS Nano*, 2022, **16**, 18058–18070.
68 S. Zhao, F. Ning, X. Yu, B. Guo, R. Teófilo, J. Huang, Q. Shi, S. Wu, W. Feng and Y. Zhao, *Angew. Chem., Int. Ed.*, 2025, **64**, e202416290.
69 S. Gao, Y. Huang, J. Geng, W. Hu, K. Feng, J. Zhong, C. Yu and F. Li, *ACS Energy Lett.*, 2025, **10**, 4140–4147.
70 T. Zhang, Z. Song, Y. Li, Y. Huang, J. Su, W. Hua and F. Li, *Angew. Chem., Int. Ed.*, 2025, **64**, e202509816.
71 H. Wang, T. Liu, H. Chen, Y. Mei, J. Gao, L. Ni, N. Hong, J. Huang, X. Hu, W. Deng, G. Zou, H. Hou, D. Silvester, C. Banks, X. Ji and K. Amine, *Nat. Commun.*, 2025, **16**, 4409.
72 X. Song, R. Liu, J. Jin, X. Zhao, Y. Wang, Q. Shen, Z. Sun, X. Qu, L. Jiao and Y. Liu, *Energy Storage Mater.*, 2024, **69**, 103377.

73 A. Zeng, N. Li, H. Zhang, S. Qiu, Z. Xu, Y. Zhang, W. Yin, E. Zhao and X. Xiao, *Angew. Chem., Int. Ed.*, 2025, **64**, e202514220.
74 Y. Yang, Z. Wang, C. Du, B. Wang, X. Li, S. Wu, X. Li, X. Zhang, X. Wang, Y. Niu, F. Ding, X. Rong, Y. Lu, N. Zhang, J. Xu, R. Xiao, Q. Zhang, X. Wang, W. Yin, J. Zhao, L. Chen, J. Huang and Y. Hu, *Science*, 2024, **385**, 744–752.